LEARNING VELOCITY PRIOR-GUIDED HAMILTONIAN-JACOBI FLOWS WITH UNBALANCED OPTIMAL TRANSPORT

Anonymous authors
Paper under double-blind review

ABSTRACT

The connection between optimal transport (OT) and control theory is well established, most prominently in the Benamou–Brenier dynamic formulation. With quadratic cost, the OT problem can be reframed as a stochastic control problem in which a density ρ_t evolves under a controlled velocity field v_t subject to the continuity equation $\partial_t \rho_t + \nabla \cdot (\rho_t v_t) = 0$. In this work, we introduce a velocity prior into the continuity equation and derive a new Hamilton–Jacobi–Bellman (HJB) formulation to learn dynamical probability flows. We further extend the approach to the unbalanced setting by adding a growth term, capturing mass variation processes common in scientific domains such as cell proliferation and differentiation. Importantly, our method requires training only a single neural network to model v_t, without the need for a separate model for the growth term g_t. Finally, by decomposing the velocity field as $v_{\text{total}} = v_{\text{prior}} + v_{\text{corr}}$, our approach is able to capture complex transport patterns that prior methods struggle to learn due to the curl-free limitation.

1 INTRODUCTION

From flow matching (FM) to action matching (AM), learning transport maps between distributions has been widely explored in recent years (Lipman et al., 2022; Albergo and Vanden-Eijnden, 2022; Liu et al., 2022; Neklyudov et al., 2023a). *Flow Matching (FM)* (Lipman et al., 2022) learns a time–dependent velocity field u_t that pushes ρ_0 to ρ_1 and can realize highly expressive transport paths; however, the original FM with independent coupling between source and target does not guarantee *least action* by minimizing the kinetic energy in the Benamou–Brenier sense. Instead, it trains u_t to match conditional expectations of displacement vectors under a chosen interpolation scheme, which may yield non-optimal flows.

Action Matching (AM) (Neklyudov et al., 2023a) addresses this by parameterizing a scalar potential s_t whose gradient ∇s_t induces the transport, aligning with the optimality conditions of OT and yielding lower kinetic energy than unconstrained FM. The price is reduced expressiveness: ∇s_t is *curl-free*, so AM cannot directly represent rotational or cyclic dynamics that are common in scientific domains. From the Helmholtz decomposition perspective (Neklyudov et al., 2023a), any vector field u_t^* can be written as $u_t^* = \nabla s_t^* + w_t$ with w_t divergence-free (Ambrosio et al., 2005, §8.4.2). Under this lens, AM retains only the gradient component and discards discards w_t, explaining both its energy efficiency and its inability to encode rotations and cycles.

In this paper, we seek a middle ground – expressive like FM, energy-aware like AM – by introducing a velocity prior v_{prior} and learning only the residual potential. We note that even compared with energy-aware FM variants such as OT–CFM(Pooladian et al., 2023; Tong et al., 2023a), our approach achieves better energy efficiency, as demonstrated in upper Table 2. Specifically, we decompose the velocity field as $v_{\text{total}}(t, x) = v_{\text{prior}}(t, x) + \nabla s_t(x)$. Here v_{prior} captures known rotational dynamics or domain-specific effects such as RNA velocity in single-cell biology, while ∇s_t accounts for the OT-consistent gradient component. We train s_t by minimizing a modified Hamilton–Jacobi residual that incorporates the prior, together with boundary terms that ensure $\rho_0 \to \rho_1$. This *residualized* design preserves OT optimality conditions for the learned component, improves interpretability,

and injects inductive bias without paying the kinetic-energy cost of unconstrained original FM. We name our approach the Velocity Prior Hamiltonian-Jacobi Flow (VP-HJF).

Motivation in practice In domains like single–cell biology and physical systems with known drifts, accurate priors are available yet incomplete and and mass change such as cell proliferation and decay is ubiquitous. VP–HJF exploits these priors to encode hard–to–learn structure. The residual potential learns both the correction that the prior can not explain and the mass changes through the growth term. This yields a compact and interpretable alternative to fully free vector–field models, particularly effective when local supervision is noisy but prior knowledge is rich.

2 BACKGROUND

Dynamical Optimal Transport Beyond the classic static Monge–Kantorovich formulation in OT (Ambrosio et al., 2005; Villani et al., 2008), there exists a dynamical formulation known as the Benamou–Brenier problem which links OT with PDEs by representing the W_2 distance as the minimum kinetic energy where ρ_t is density and v_t is a velocity field with boundary conditions: $\rho_{|t=0} = \rho_0$, $\rho_{|t=1} = \rho_1$, (Benamou and Brenier, 2000):

$$W_2^2(\rho_0, \rho_1) = \inf_{\rho_t, v_t} \int_0^1 \int \tfrac{1}{2}\|v_t(x)\|^2 \rho_t(x)\, dx\, dt, \quad \partial_t \rho_t + \nabla \cdot (\rho_t v_t) = 0. \tag{1}$$

Unbalanced Optimal Transport When total mass change over time such as following a growth-decay process in biology, we add a growth rate $g_t(x)$ term to the continuity equation to incorporate the weight changes (Chizat et al., 2018):

$$\partial_t \rho_t(x) + \nabla \cdot \big(\rho_t(x)\, v_t(x)\big) = g_t(x)\, \rho_t(x), \quad \rho_{|t=0} = \rho_0, \; \rho_{|t=1} = \rho_1, \tag{2}$$

The Wasserstein–Fisher–Rao distance with scale $\delta > 0$ is defined as the minimal action balancing transport cost and mass change:

$$\mathrm{WFR}_\delta^2(\rho_0, \rho_1) = \inf_{\rho, v, g} \int_0^1 \int \left(\tfrac{1}{2}\|v_t(x)\|^2 + \tfrac{\delta^2}{2} g_t(x)^2 \right) \rho_t(x)\, dx\, dt, \quad \text{s.t. } Eq.2. \tag{3}$$

Hamilton–Jacobi–Bellman (HJB) We recall the classical connection between optimal control and Hamilton–Jacobi (HJ) theory. Consider a deterministic control system with state $x(t) \in \mathbb{R}^d$, control $u(t)$, dynamics $\dot{x} = f(x, u, t)$, running cost $L(x, u, t)$, and terminal cost $\psi(x)$. The *value function*

$$V(t, x) = \inf_{u(\cdot)} \left\{ \int_t^1 L\big(x(s), u(s), s\big)\, ds + \psi\big(x(1)\big) \right\}$$

gives the minimal cost-to-go from (t, x) under admissible controls. It is well known that V solves the Hamilton-Jacobi-Bellman (HJB) PDE

$$\partial_t V(t, x) + H\big(x, \nabla V(t, x), t\big) = 0, \quad V(1, x) = \psi(x),$$

where the Hamiltonian is

$$H(x, p, t) := \inf_u \left\{ L(x, u, t) + p^\top f(x, u, t) \right\}, \qquad p = \nabla V(t, x).$$

Action Matching (AM) AM fits a scalar potential s_θ to learn a energy-minimizing flow between distributions by minimizing the (un)balanced HJB residuals.

$$\mathcal{L}_{\mathrm{uAM}} = \int_0^1 \mathbb{E}_{x \sim \rho_t} \left[\partial_t s_\theta(t, x) + \tfrac{1}{2}\|\nabla_x s_\theta(t, x)\|^2 + \frac{1}{2} s_\theta^2(t, x) \right] dt, \tag{4}$$

with boundary constraints as: $\mathbb{E}_{x \sim \rho_0}[s_0(x)] - \mathbb{E}_{x \sim \rho_1}[s_1(x)]$.

3 METHODOLOGY

We introduce a velocity-prior guided approach, the *Velocity Prior Hamiltonian–Jacobi Flow (VP-HJF)*, to solve the unbalanced optimal transport problem under the Wasserstein–Fisher–Rao (WFR) metric (Eq. 2, 3). In contrast to prior approaches that fit two separate networks—one for transport and one for growth (Zhang et al., 2024; Wang et al., 2025), our method trains a single neural network. Following (Neklyudov et al., 2023a), we can represent both the transport velocity field and the growth term through a single scalar potential.

Proposition 3.1 (Neklyudov et al., 2023a, Prop. 3.3). *Suppose we have a continuous dynamic flow with density ρ_t. Under mild conditions, there exists a unique scalar potential function $\hat{s}_t(x)$ such that the unbalanced continuity equation (2) is satisfied, with the velocity field and growth function given by $v_t^*(x) = \nabla \hat{s}_t(x), g_t^*(x) = \hat{s}_t(x)$.*

Building on Proposition 3.1, we reduces the WFR problem to learning a single model and incorporate problem-specific dynamics through a simple velocity decomposition. Specifically, we decompose the velocity field into two parts: a known velocity prior and a learnable corrective velocity field component:

$$v_{\text{total}}(t,x) = v_{\text{prior}}(t,x) + v_{\text{corr}}(t,x), \tag{5}$$

where v_{prior} encodes domain knowledge (e.g. translations, rotations, RNA velocity), and v_{corr} is the is the data–driven corrective component. In this way, the prior captures coarse dynamics while the model focuses on refinements such as correcting the residual transport and learning mass imbalance that the prior cannot explain. In essence, our approach improves interpretability and reduces the learning complexity through adding prior knowledge of the velocity field v_{prior} – leaving the learnable velocity field v_{corr} simpler learning tasks compared with other generative modeling methods of learning the entire velocity field v_{total}. Intuitively, our approach pays kinetic cost only for the *correction* to the prior drift and for the mass growth-decay component, making learning more efficient.

We can now define our velocity-prior guided unbalanced OT problem under the least-action principle as:

Definition 3.2. Consider the following least-action objective with $\delta=1$ and subject to the unbalanced *velocity-prior guided* continuity equation :

$$\mathcal{A}(\rho, v, g) = \int_0^1 \int \left(\tfrac{1}{2}\|v(t,x)\|^2 + \tfrac{1}{2}g(t,x)^2 \right) \rho_t(x) \, dx \, dt, \tag{6}$$

$$\text{s.t.} \quad \partial_t \rho_t = -\nabla \cdot \left(\rho_t \left(v_{\text{prior}} + v_{\text{corr}} \right) \right) + g_t \, \rho_t, \quad \rho_{|t=0} = \rho_0, \ \ \rho_{|t=1} = \rho_1. \tag{7}$$

Note that in our method we do *not* optimize over ρ directly. Instead, ρ_t is *induced* by a parametric flow Φ_t^θ via $\dot{x} = v_{\text{prior}}(t,x) + \nabla s_\theta(t,x)$ and defined as $\rho_t^\theta = (\Phi_t^\theta)_{\#}\rho_0$.

Prior-guided HJB residual Since solving for the minimum-action problem in primal form in Definition 3.2 is intractable, we turn to its dual formulation. The key derivation step is to introduce a scalar potential $s(t,x)$ as the Lagrange multiplier for the prior-guided continuity equation and applying the Fenchel–Young inequalities to the velocity field and growth term. We then obtain the following dual lower bound (see Appendix A for details):

$$\mathcal{A}(\rho, v, g) \geq \mathbb{E}_{\rho_0(x)}[\, s_0(x) \,] - \mathbb{E}_{\rho_1(x)}[\, s_1(x) \,]$$
$$- \int_0^1 \int \rho_t(x) \left(\partial_t s + \tfrac{1}{2}\|\nabla s\|^2 + \nabla s \cdot v_{\text{prior}} + \tfrac{1}{2}s^2 \right) dx \, dt. \tag{8}$$

The bound is tight point-wise if and only if when we choose the primal variables as

$$v_{\text{corr}}(t,x) = \nabla_x s(t,x), \qquad g(t,x) = s(t,x),$$

which shows that s can simultaneously control both the *corrective* transport $\nabla_x s$ and the local growth s. We can then plug these back to the continuity equation to get the optimal particle dynamics and their log-weights evolve as

$$\dot{x}(t) = v_{\text{total}}(t,x) = v_{\text{prior}}(t,x) + \nabla_x s(t,x), \qquad \frac{d}{dt} \log w(t) = s(t,x(t)).$$

Corollary 3.3 (HJB residual objective). *Motivated by the duality form, we propose to parameterize $s_\theta(t, x)$ with a neural network and define the* velocity-prior guided HJB residual *as:*

$$r_\theta(t, x) := \partial_t s_\theta(t, x) + \tfrac{1}{2}\|\nabla_x s_\theta(t, x)\|^2 + \nabla_x s_\theta(t, x) \cdot v_{\text{prior}}(t, x) + \tfrac{1}{2} s_\theta(t, x)^2. \tag{9}$$

Then minimizing

$$\mathcal{L}_{\text{HJB}}(\theta) = \mathbb{E}_{\rho_0(x)}[s_0] - \mathbb{E}_{\rho_1(x)}[s_1] + \int_0^1 \mathbb{E}_{\rho_t(x)}\big[w(t, x)r_\theta(t, x)^2\big]\, dt \tag{10}$$

drives s_θ toward dual feasibility. Note that in practice, we use squared residual to prevent positive and negative values from cancellation and add a importance weight $w(t)$ trick to reduce variance.

Importance Reweighting   The squared HJB residual can be dominated by a few high-variance outliers (rare cells, sharp local flows), which destabilizes training. To ensure training stability and preventing these extreme high residual outliers, we adopt a simple batch-wise importance reweighting that down-weights large residuals. For a mini-batch $\{(t_i, x_i)\}_{i=1}^B$, let $r_i = \big|r_\theta(t_i, x_{t,i})\big| + \varepsilon$ and with a temperature $\tau > 0$. Then for each sample, the weight is inversely proportions to a temperature-shaped residual as $\tilde{w}_i \propto r_i^{-\tau}$. Thus, larger residuals get smaller weight, which reduces variance while keeping the update focused and stable.

Theorem 3.4 (Prior-guided HJB optimality). *Suppose that the HBJ residual defined in corollary.3.3 satisfies $r_\theta(t, x) = 0$ for ρ_t-a.e on $[0, 1]\times\mathbb{R}^d$, and the boundary constraints hold, then $(\rho_t, v_{\text{total}}, g_\theta)$ satisfies the unbalanced continuity equation and the WFR optimality conditions in Definition 3.2. In particular, the learned corrective field $v_{\text{corr}}^* = \nabla_x s_\theta$ and growth $g^* = g_\theta$ satisfy the optimality conditions.*

While the HJB residual enforces local optimality conditions, it does not guarantee that the terminal distribution ρ_1^θ matches with the target ρ_1. To bridge this gap, we design a two-part reconstruction objective: (i) a density matching term through the sliced Wasserstein between the predicted $\hat{\rho}_1$ and ρ_1, and (ii) a mass term aligning the global log-mass ratio. These two terms directly calibrates the terminal distribution's *shape* and *mass*, complementing the HJB residual.

Reconstruction loss   To align the terminal distribution in *shape*, we use a sliced Wasserstein objective. Let $\hat{\rho}_1$ be the empirical terminal distribution learned from our model, and ρ_1 be the ground truth target distribution. θ_ℓ is a random projection sampled from $\theta_\ell \sim \text{Unif}(\mathbb{S}^{d-1})$ for $\ell = 1, \ldots, L$, $\hat{X}_1$ are predicted samples, and Y are ground-truth samples, the sliced Wasserstein loss is defined as:

$$\text{SW}_2^2(\hat{\rho}_1, \rho_1) \approx \frac{1}{L}\sum_{\ell=1}^L W_2^2\Big(\langle\theta_\ell, \hat{X}_1\rangle, \langle\theta_\ell, Y\rangle\Big), \tag{11}$$

where W_2^2 on $\mathbb{R}$ is the 1D Wasserstein distance computed by sorting projections.

To capture *global mass change*, we integrate particle log–weights along the learned dynamics. With WFR scale $\delta = 1$ and a mini-batch of size B. At $t = 0$, we initialize the weights as $\log w_i(0) = 0$, and follow the below characteristic ODEs to calculate the predicted terminal mass ratio at $t = 1$ relative to $t = 0$:

$$\frac{d}{dt}\log w_i(t) = s_\theta\big(t, x_i(t)\big), \qquad \hat{r} = \frac{1}{B}\sum_{i=1}^B e^{\log w_i(1)} = \{\log w_i(1)\}_{i=1}^B \tag{12}$$

We penalize against the ground truth ratio r via its logarithmic form to ensure stability and enforces the WFR consistency: $\mathcal{L}_{\text{mass.}} = \big(\log\hat{r} - \log r\big)^2$. Our final reconstruction loss combines the two components with tunable coefficients:

$$\mathcal{L}_{\text{recon}} = \lambda_{\text{sw}}\, \text{SW}_2^2(\hat{\rho}_1, \rho_1) + \lambda_{\text{mass}}\big(\log\hat{r} - \log r\big)^2 \tag{13}$$

with $\lambda_{\text{sw}} > 0$ and $\lambda_{\text{mass}} > 0$. In practice we use $L \in [64, 512]$ random projections, and choose $\lambda_{\text{mass}} \in [0.1, 1]$ to calibrate mass without overpowering other terms.
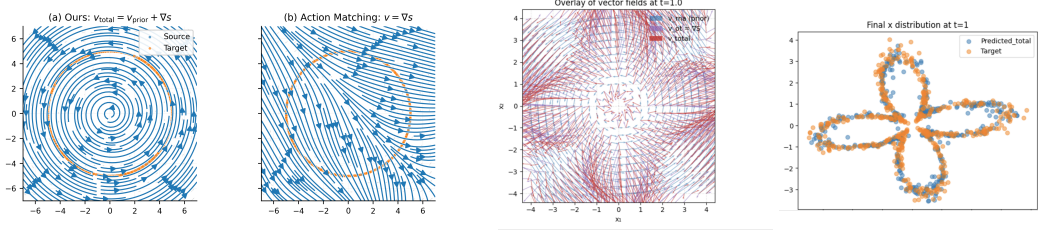
Figure 1: **Left** (first two): Ours correctly learned the rotating dynamic while AM failed. **Middle**: Vector field (red) bending away from v_{prior} (blue) to form petal shapes. **Right**: Predicted target distribution matches with ground truth

Total objective Putting the pieces together, our total training loss is

$$
\min_\theta \ \mathcal{L}(\theta) = \underbrace{\mathbb{E}_{x\sim\rho_0}[s_0(x)] - \mathbb{E}_{x\sim\rho_1}[s_1(x)] + \int_0^1 \mathbb{E}_{x\sim\rho_t}\big[w(t,x)\,r_\theta(t,x)^2\big]\,dt}_{\mathcal{L}_{\text{HJB}}} \tag{14}
$$

$$
+ \underbrace{\lambda_{\text{sw}}\,\text{SW}_2^2(\hat\rho_1,\rho_1) + \mathcal{L}_{\text{mass}}}_{\mathcal{L}_{\text{recon}}}
$$

where $r_\theta(t,x)$ is the HJB residual, $w(t,x)$ are the nonnegative weights, and $\hat\rho_1(\theta)$ is the terminal distribution obtained by pushing ρ_0 through the learned dynamics.

4 RELATED WORKS

Physics-constrained approach Existing works (Koshizuka and Sato, 2022; Neklyudov et al., 2023b; Tong et al., 2020) add a *potential-based prior* $V_t(x)$ to the HJ equation to incorporate prior knowledge for trajectory inference. In (Neklyudov et al., 2023b), this yields $\partial_t s + \frac{1}{2}\|\nabla s\|^2 + V_t + \frac{1}{2\delta^2}s^2 = 0$ and the conservative second–order law $\ddot{X}_t = -\nabla V_t(X_t)$. Meanwhile, our method is the *velocity-based prior* approach, the known velocity field v_{prior} enters as a drift inside the continuity equation, which produces the cross-term $\nabla s \cdot v_{\text{prior}}$. Since potential-based priors is curl-free, it can not represent rotational flows as in (Neklyudov et al., 2023a); By contrast, our data-driven formulation uses a flexible measured vector fields directly as v_{prior}, which can be considered as a "free drift" and learns only minimal optimal corrections and growth.

Other trajectory inference approaches. Trajectory inference has also advanced through *flow matching* and *Schrödinger bridge* methods, which scale effectively to high-dimensional data. Recent SB variants further improve performance on single-cell datasets include (Huguet et al., 2022; Tong et al., 2023b). For unbalanced settings, variational and regularized UOT methods such as DeepRUOT, VRUOT, and VGFM directly learn transport dynamics and growth from snapshot data (Zhang et al., 2024; Sun et al., 2025; Wang et al., 2025). In particular, VRUOT also uses a single network to model both the velocity field and the growth term, but it did not incorporate prior known knowledge like ours.

5 EXPERIMENTS

5.1 SYNTHETIC DATASET

Balanced case - Rotating Ring First, we show a case when utilizing the velocity prior is crucial in learning the correct velocity field where curl-free methods like AM fails. We tested on a 2D rotating ring dataset where the points on the ring (source) are rotated by a fixed angle θ (target). The velocity prior is defined as $v_{\text{prior}} = \omega J x$, where J is the skew-symmetric rotation matrix and $x \in \mathbb{R}^2$, so this becomes $Jx = \begin{bmatrix} 0 & 1; & -1 & 0 \end{bmatrix}\begin{bmatrix} x_1 & x_2 \end{bmatrix}^\top = (-x_2,\, x_1)^\top$. The task for our model v_{ot} is to

Method	$\mathbf{W_2}$	Control action (∇s)	Total kinetic (v_{total})
Flow Matching	0.582	18.369	18.369
OT–FM	**0.402**	18.707	18.707
VP–HJF (Ours)	0.577	**0.624**	**17.955**
Prior-only ($\alpha{=}1$)	1.351	0	36.250

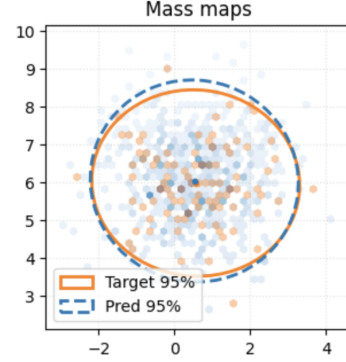| Method	r_{pred}	$|\Delta \log r|$	Rel. % err.
VP–HJF (ours)	1.356	0.044	4.30%
VP–HJF (w/o $\mathcal{L}_{\text{mass}}$)	0.899	0.455	36.56%
Unbalanced AM	0.938	0.413	33.80%

Figure 2: **Left:** Upper table on Least Action Comparison for Balanced Gaussian Translation; *Bottom table:* Effect of the mass loss $\mathcal{L}_{\text{mass}}$. r_{pred} is the predicted mass ratio , the absolute log error $|\Delta \log r| = |\log r_{\text{pred}} - \log r_{\text{true}}|$, and the relative error (%), with $r_{\text{true}} = 1.418$. **Right:** Ellipses shows the mean/covariance of our approach matches with Target for Unbalanced Gaussian Translation; Inside, each bin indicates weights. see Appendix B

learn the residual correction after given the prior rotation knowledge, such as ensuring the boundary condition by aligning the mismatched source and target density or correcting the radial drift by push the points inwards or outwards,etc. In Figure 1 left (b), we show that since AM has the curl-free limitation, without a prior, its model $\nabla s_t(x)$ failed to represent pure rotation where the streamlines cut through the circle. In Figure 1 left (a), the streamlines from our method form a circular flow indicating that v_{prior} gives the model the correct inductive bias.

Diverging Petal We created a curved and rotated petal-shape dataset to test our method on diverging multi-trajectory paths. The source is a gaussian distribution concentrated in the center and $v_{\text{prior}=\omega Jx}$ the rotation dynamic defined as before. Our task is to learn v_{petal}, a radial and angle-dependent term that push outward the points along the radius with different speed depend on the angle $\theta = \text{atan2}(y, x)$. We have

$$v_{\text{petal}}(x) = s(\theta)\hat{r}, \quad \hat{r} = \frac{x}{\|x\|}, \quad s(\theta) = \max\big(0,\ b + a\cos(k\theta)\big) \qquad (15)$$

Compared with the petal shape appeared in AM and MioFlow (Huguet et al., 2022), the underlying dynamic flow in our example is harder to learn, where the former one has a straight-axis aligned radial expansion as $r(x) = |x_1| + |x_2|$ with the gradient of $r(x)$ being a piece-wise constant and curl-free. Figure 1 middle shows that our petal shape matches with the target shape. Figure 1 right shows that the vector field (red arrows) are bending away from pure rotation (blue arrows) to align strongly with the petal shape by pushing the mass outward.

Balanced case - Gaussian Translation In this experiment, we compare the least-action or energy costs across different methods. As shown in Table 2(upper), our proposed VP–HJF achieves Wasserstein distance W_2 accuracy on par with FM Lipman et al. (2022) while OT-FM Tong et al. (2023a); Pooladian et al. (2023) attains the lowest Wasserstein distance. By contrast, both FM and OT-FM must learn the entire velocity field $u_t = \nabla s + w_t$, resulting in a much larger control action. This demonstrates that VP–HJF leverages the structured prior effectively, where the prior dynamics carry most of the transport, and the learned correction ∇s makes adjustments. To verify that our improvement is not solely due to a strong velocity prior v_{prior} itself, we also report a prior-only baseline. The prior alone shows moderate accuracy but with high kinetic cost, whereas our method is able to balance both accuracy and energy efficiency. Additionally, Fig. 1 highlights that incorporating the velocity prior is crucial in the rotational dynamics setting, as well as in a multi-trajectory example where paths diverge into a petal shape.

Lotka–Volterra with growth. We model the prey and predator densities $x_1(t), x_2(t)$ by a first–order nonlinear ODE,

$$\dot{x}_1(t) = \alpha\, x_1(t) - \beta\, x_1(t)\, x_2(t), \qquad \dot{x}_2(t) = -\gamma\, x_2(t) + \delta\, x_1(t)\, x_2(t),$$

$\Delta \log r$ (abs) $\downarrow$	Clean	Gaussian noise α		Scale c		Wrong coeff	
		0.5	0.75	0.50	0.75	medium	hard
VP-HJF (ours)	0.04	0.17	0.14	0.02	0.11	0.21	0.37
Prior-only†	0.35	0.35	0.35	0.35	0.35	0.35	0.35

Table 1: Ablations on prior robustness (LV). The absolute $\Delta \log r := \big| \log \hat{r} - \log r \big|$. Prior-only corresponds to the ground truth mass ratio (mass-conserving). Wrong coeff medium uses $\alpha = 1.3, \beta = 0.8, \gamma = 1.2, \delta = 0.7$ and hard uses $\alpha = 1.5, \beta = 0.6, \gamma = 1.4, \delta = 0.6$

Algorithm 1 Training VP–HJF (Velocity-Prior Hamiltonian–Jacobi Flow)

Require: per time-interval t_k snapshots $\{x, t_k, v_k^{prior}\}_{k=0}^K$, network $s_\theta(t, x)$, coefficients $\alpha, \beta, \lambda_{\mathrm{SW}}, \lambda_{\mathrm{mass}}$,

1: **while** not converged **do**
2:     Sample interval index $k \in \{0, \ldots, K-1\}$,
3:     Sample adjacent pairs $(x_k^{(b)}, v_k^{(b)}, x_{k+1}^{(b)}, v_{k+1}^{(b)})_{b=1}^B \sim \{x, t, v_{prior}\}_{k=0}^K$
4:     Sample normalized $t \sim (0, 1)$
5:     **HJB residual loss:**
6:     Compute $s_k \leftarrow s_\theta(t_k, x_k)$, $s_0 \leftarrow s_\theta(t_0, x_k)$, $s_1 \leftarrow s_\theta(t_1, x_{k+1})$;
7:     Compute importance weights $w_b \propto r_{k,b}^{-\tau}$
8:     $r_k \leftarrow \partial_t s_k + \frac{1}{2} \|\nabla_x s_k\|^2 + \nabla_x s_k \cdot v_{\mathrm{prior}}(t_k, x_k) + \frac{1}{2} s_k^2$
9:     $\mathcal{L}_{\mathrm{HJB}} \leftarrow \mathbb{E}_{\rho_{t_0}}[s_0] - \mathbb{E}_{\rho_{t_1}}[s_1] + \frac{1}{B} \sum_{b=1}^B w_b \, r_{k,b}^2$
10:    **Reconstruction loss:**
11:    Initialize particles $x^{(b)} \leftarrow x_k^{(b)}$ and $\log w^{(b)} \leftarrow 0$ for $b = 1..B$
12:    ode rhs $= \big[\dot{x} = \nabla_x s_\theta(t, x) + v_{\mathrm{prior}}(t, x), \ \dot{\log w} = s_\theta(t, x) \big]$
13:    $(x_{k+1}^{\mathrm{pred}}, \log w_{k+1}) \leftarrow \texttt{odeint}\Big(\text{ode rhs}, (x_k, \mathbf{0}), \ t \in [t_k, t_{k+1}] \Big)$
14:    **Sliced Wasserstein loss:** $\mathcal{L}_{\mathrm{SW}} \leftarrow \frac{1}{L} \sum_{\ell=1}^L W_2^2(x_{k+1}^{\mathrm{pred}}, x_{k+1})$
15:    **Mass loss:** $\mathcal{L}_{\mathrm{mass}} \leftarrow (\log \hat{w}(1) - \log w(1))^2$
16:    $\mathcal{L}_{\mathrm{recon}} \leftarrow \lambda_{\mathrm{SW}} \mathcal{L}_{\mathrm{SW}} + \lambda_{\mathrm{mass}} \mathcal{L}_{\mathrm{mass}}$
17:    **Total loss:** $\mathcal{L}(\theta) \leftarrow \alpha \mathcal{L}_{\mathrm{HJB}} + \beta \mathcal{L}_{\mathrm{recon}}$
18:    Update $\theta \leftarrow \theta - \eta \nabla_\theta \mathcal{L}(\theta)$
19: **end while**

---

where α is the prey's intrinsic growth rate, β is the predation rate, γ is the predator's mortality rate, and δ is the predator's growth rate from consuming prey. To model the population expansion and decay dynamics, we use a simple scalar growth field and evolve local mass via the weight dynamics

$$g\big(x(t)\big) = \kappa \big(x_1(t) - x_2(t)\big), \quad \frac{d}{dt} \log w(t) = g\big(x(t)\big)$$

The total mass $M(t) = \mathbb{E}[w(t)]$ and the ground-truth mass ratio is calculated as $r_{\mathrm{true}} = M(t)/M(0)$.

Table 2 (bottom) shows that adding the explicit mass term $\mathcal{L}_{\mathrm{mass}}$ enables our method to closely match r_{true} with 4% of relative error while both unbalanced AM and our method without the $\mathcal{L}_{mass}$ term suffer from a much higher relative error of over 30%. Although AM aligns transport but leaves the *scale* of the scalar potential s_θ unconstrained, so the integrated growth $\int_0^t g(x(t)) \, dt$ is miscalibrated. By contrast, $\mathcal{L}_{\mathrm{mass}}$ provides endpoint constraint on the mass – yielding better mass dynamics and more aligned with the ground truth mass ratio.

Ablations on prior robustness   In this section, we conduct various ablation studies to test the robustness of our model. In particular, we modify the quality of v_{prior} by misspecifying it to different scaling $v_{\mathrm{prior}} = cv$, adding Gaussian noises $v_{\mathrm{prior}} = v + \eta$ and using the wrong coefficients with various level of difficulties in the LV equation. We compare it with the prior-only approach which

Table 2: Comparison on the EB dataset using SWD at the held-out marginals (t_1, t_3) and the mean over the remaining snapshots. Baseline results are taken from (Theodoropoulos et al., 2025)

Method	SWD t_1	SWD t_3	Rest SWD
SBIRR	0.80 ± 0.06	0.91 ± 0.05	0.66 ± 0.07
MMFM	0.59 ± 0.04	0.76 ± 0.04	0.52 ± 0.07
DMSB	0.58 ± 0.06	0.54 ± 0.06	0.45 ± 0.04
3MSBM	0.48 ± 0.04	$\mathbf{0.38 \pm 0.03}$	$\mathbf{0.36 \pm 0.05}$
VP-HJF (ours)	$\mathbf{0.37 \pm 0.01}$	0.46 ± 0.01	0.50 ± 0.08

essentially corresponds to the ground-truth mass ratio r_{true} as mass is conserved in this case. Table 1 shows that under global scaling our approach is particularly stable – indicating that the learned corrective field v_{corr} and growth term calibrate mass well when the prior's direction is correct up to scale. With additive Gaussian perturbations, errors remain modest showing tolerance to stochastic mis-specification. The primary failure is the wrong coefficient (hard)case, which reflects the sensitivity to severe directional mismatch that cannot be fully compensated without incurring large kinetic corrections.

5.2 REAL-WORLD DATASET

In this section, we evaluate our method on two single-cell RNA-seq datasets. Both provide RNA velocity, which we use as the velocity prior v_{prior}. Such priors are common in biological and scientific applications beyond single-cell data. Incorporating them introduces an inductive bias that reduces learning complexity — our model needs only to learn a corrective flow and growth rather than the full dynamics from scratch.

EB scRNA-Seq data   We evaluate cell-trajectory inference on the Embryoid Body (EB) dataset of Moon et al. (2019), using the preprocessed release from Koshizuka and Sato (2022); Tong et al. (2020). The dataset comprises five snapshots over 27 days, grouped as $t_0 \in [0, 3]$, $t_1 \in [6, 9]$, $t_2 \in [12, 15]$, $t_3 \in [18, 21]$, $t_4 \in [24, 27]$. Leveraging RNA velocity as a prior v_{prior} at each snapshot, we train a local and shorter trajectory by adopting the *local per-interval* training: at each step we sample an adjacent pair (t_k, t_{k+1}) and learn only the transport and growth to move $\rho_{t_k} \to \rho_{t_{k+1}}$. This yields more stable gradients and low target variance than enforcing all time points jointly;. For details of the training algorithm, see Algorithm 1.

We test on 100-dim PCA components feature space and compare with recent works using the multi-marginal approach from 3MSBM(Theodoropoulos et al., 2025), SBIRR (Shen et al., 2024), MMFM (Rohbeck et al., 2025) and DMSB (Chen et al., 2023). We follow the experiment setup from 3MSBM by having $t = 1, 3$ as the held out sets. Table 2 shows that our method outperforms others at $t = 1$ and remains competitive at other time snapshots in sliced Wasserstein distance. Notably, our method outperforms SBIRR and MMFM which solve a piecewise Schrödinger Bridges and OT coupling instead of a single global optimization with a joint coupling like 3MSBM and DMSB, indicating the benefits of using RNA velocity as a local prior with per-interval supervision.

Bone marrow scRNA-Seq data   We evaluate our approach on a real scRNA-seq bone-marrow atlas with multiple hematopoietic fates from scVelo (Bergen et al., 2020). Figure 3 (left) shows trajectories that emanates from early progenitor regions at $t{=}0$ (dark blue) and spread out to other branches by closely following the UMAP reference (gray). Figure 3 (right) shows the learned growth field $g_\theta(t, x) = s_\theta(t, x)$ that governs local mass dynamics. This maps shows that our model successfully captured low growth rate in early progenitors and increases as cells enter the active cycling and amplification stage. However, we also observe that the high growth rate near some terminal regions. While this indicates the model can assign higher growth to specific cell types, a strong terminal-phase growth is biologically implausible. For the bone marrow case, mature or exiting cells should have near-zero or negative growth. This likely reflect the objective imbalance where transport terms dominating mass calibration, suggesting mild regularization such as time-smoothness on s_θ or branch-wise boundary constraints to better align growth with biology.
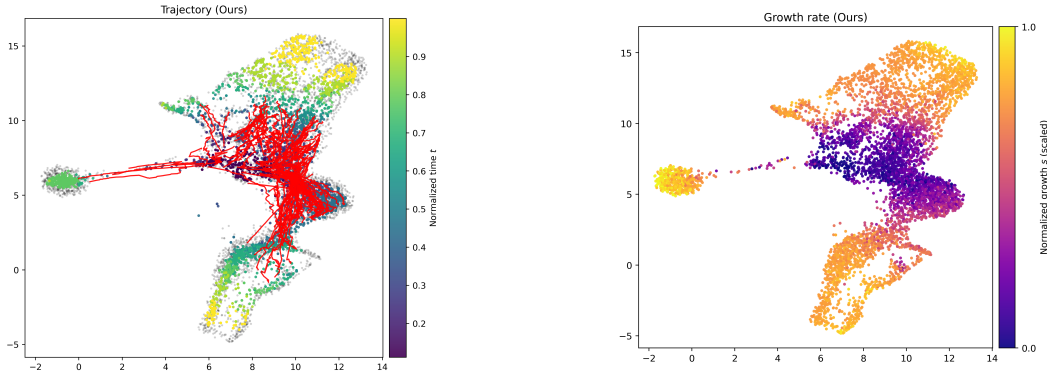
Figure 3: **Left**:Bone marrow trajectories. Colored points (ours) show inferred cell trajectories overlaid on the reference manifold (gray)) **Right**: Learned growth field — orange means high growth, purple means low growth.

6 DISCUSSION AND LIMITATIONS

On the velocity prior quality and assumptions The velocity prior v_{prior} indeed plays a constructive—but double-edged role in our method. A good prior captures coarse dynamics - reducing the learning complexity and improving on sample efficiency. A misspecified prior can bias the learned corrective field $s_\theta(t, x)$ and slow or destabilize training. Hence, the *quality* of v_{prior} strongly influences both optimization and generalization. In practice, mild perturbation of the prior through noise, scale or misspecification are corrected by s_θ, whereas severe misspecification such as overly large or structurally wrong drifts can bias the learned corrective flow as tested in our ablation studies Table 1. Moreover, v_{prior} does *not* require divergence-free assumption. Our dual objective explicitly includes the cross term $\nabla_x s_\theta \cdot v_{\text{prior}}$ in the HJB residual avoiding hidden orthogonality requirements.

Limitations In Fig. 3 (right) we observe high growth near terminal regions, which is biologically implausible for mature or cell–cycle–exiting states. Without additional biological constraints such as cell-cycle markers,branch–terminal boundary conditions or proliferation markers, growth–transport disentanglement may remain underdetermined in some regions. A promising direction is to add weak supervision on the learned growth model to improve identifiability.

For single–cell datasets we currently use local supervision—training on adjacent pairs with a time–continuous shared network. This choice is simple and scalable and induces a globally smooth field, but it does not jointly enforce all marginals as in recent multi–marginal methods, which may limit long–range trajectory coherence. In future works, extending VP–HJF with global consistency could improve on long-range trajectory inference.

7 CONCLUSION

Our method decomposes the velocity field to embed domain knowledge for better energy efficiency and uses a single network to capture both unbalanced growth and transport.

REFERENCES

Yaron Lipman, Ricky TQ Chen, Heli Ben-Hamu, Maximilian Nickel, and Matt Le. Flow matching for generative modeling. *arXiv preprint arXiv:2210.02747*, 2022.

Michael S Albergo and Eric Vanden-Eijnden. Building normalizing flows with stochastic interpolants. *arXiv preprint arXiv:2209.15571*, 2022.

Xingchao Liu, Chengyue Gong, and Qiang Liu. Flow straight and fast: Learning to generate and transfer data with rectified flow. *arXiv preprint arXiv:2209.03003*, 2022.

Kirill Neklyudov, Rob Brekelmans, Daniel Severo, and Alireza Makhzani. Action matching: Learning stochastic dynamics from samples. In *International conference on machine learning*, pages 25858–25889. PMLR, 2023a.

Luigi Ambrosio, Nicola Gigli, and Giuseppe Savaré. *Gradient flows: in metric spaces and in the space of probability measures*. Springer, 2005.

Aram-Alexandre Pooladian, Heli Ben-Hamu, Carles Domingo-Enrich, Brandon Amos, Yaron Lipman, and Ricky TQ Chen. Multisample flow matching: Straightening flows with minibatch couplings. *arXiv preprint arXiv:2304.14772*, 2023.

Alexander Tong, Kilian Fatras, Nikolay Malkin, Guillaume Huguet, Yanlei Zhang, Jarrid Rector-Brooks, Guy Wolf, and Yoshua Bengio. Improving and generalizing flow-based generative models with minibatch optimal transport. *arXiv preprint arXiv:2302.00482*, 2023a.

Cédric Villani et al. *Optimal transport: old and new*, volume 338. Springer, 2008.

Jean-David Benamou and Yann Brenier. A computational fluid mechanics solution to the monge-kantorovich mass transfer problem. *Numerische Mathematik*, 84(3):375–393, 2000.

Lenaic Chizat, Gabriel Peyré, Bernhard Schmitzer, and François-Xavier Vialard. Unbalanced optimal transport: Dynamic and kantorovich formulations. *Journal of Functional Analysis*, 274(11): 3090–3123, 2018.

Zhenyi Zhang, Tiejun Li, and Peijie Zhou. Learning stochastic dynamics from snapshots through regularized unbalanced optimal transport. *arXiv preprint arXiv:2410.00844*, 2024.

Dongyi Wang, Yuanwei Jiang, Zhenyi Zhang, Xiang Gu, Peijie Zhou, and Jian Sun. Joint velocity-growth flow matching for single-cell dynamics modeling. *arXiv preprint arXiv:2505.13413*, 2025.

Takeshi Koshizuka and Issei Sato. Neural lagrangian schr\" odinger bridge: Diffusion modeling for population dynamics. *arXiv preprint arXiv:2204.04853*, 2022.

Kirill Neklyudov, Rob Brekelmans, Alexander Tong, Lazar Atanackovic, Qiang Liu, and Alireza Makhzani. A computational framework for solving wasserstein lagrangian flows. *arXiv preprint arXiv:2310.10649*, 2023b.

Alexander Tong, Jessie Huang, Guy Wolf, David Van Dijk, and Smita Krishnaswamy. Trajectorynet: A dynamic optimal transport network for modeling cellular dynamics. In *International conference on machine learning*, pages 9526–9536. PMLR, 2020.

Guillaume Huguet, Daniel Sumner Magruder, Alexander Tong, Oluwadamilola Fasina, Manik Kuchroo, Guy Wolf, and Smita Krishnaswamy. Manifold interpolating optimal-transport flows for trajectory inference. *Advances in neural information processing systems*, 35:29705–29718, 2022.

Alexander Tong, Nikolay Malkin, Kilian Fatras, Lazar Atanackovic, Yanlei Zhang, Guillaume Huguet, Guy Wolf, and Yoshua Bengio. Simulation-free schr\" odinger bridges via score and flow matching. *arXiv preprint arXiv:2307.03672*, 2023b.

Yuhao Sun, Zhenyi Zhang, Zihan Wang, Tiejun Li, and Peijie Zhou. Variational regularized unbalanced optimal transport: Single network, least action. *arXiv preprint arXiv:2505.11823*, 2025.

Kevin R Moon, David Van Dijk, Zheng Wang, Scott Gigante, Daniel B Burkhardt, William S Chen, Kristina Yim, Antonia van den Elzen, Matthew J Hirn, Ronald R Coifman, et al. Visualizing structure and transitions in high-dimensional biological data. *Nature biotechnology*, 37(12):1482–1492, 2019.

Panagiotis Theodoropoulos, Augustinos D Saravanos, Evangelos A Theodorou, and Guan-Horng Liu. Momentum multi-marginal schr\" odinger bridge matching. *arXiv preprint arXiv:2506.10168*, 2025.

Yunyi Shen, Renato Berlinghieri, and Tamara Broderick. Multi-marginal schr\" odinger bridges with iterative reference refinement. *arXiv preprint arXiv:2408.06277*, 2024.

Martin Rohbeck, Edward De Brouwer, Charlotte Bunne, Jan-Christian Huetter, Anne Biton, Kelvin Y Chen, Aviv Regev, and Romain Lopez. Modeling complex system dynamics with flow matching across time and conditions. In *The Thirteenth International Conference on Learning Representations*, 2025.

Tianrong Chen, Guan-Horng Liu, Molei Tao, and Evangelos Theodorou. Deep momentum multi-marginal schrödinger bridge. *Advances in Neural Information Processing Systems*, 36:57058–57086, 2023.

Volker Bergen, Marius Lange, Stefan Peidli, F. Alexander Wolf, and Fabian J. Theis. Generalizing rna velocity to transient cell states through dynamical modeling. *Nature Biotechnology*, 38(12):1408–1414, August 2020. ISSN 1546-1696. doi: 10.1038/s41587-020-0591-3. URL http://dx.doi.org/10.1038/s41587-020-0591-3.

A PRIOR-GUIDED HJB INEQUALITY DERIVATION

To derive the velocity-prior guided HJB residual inequality in Eq.8.

$$\mathcal{A}(\rho, v, g) \ \geq \ \mathbb{E}_{x \sim \rho_0}[s_0(x)] - \mathbb{E}_{x \sim \rho_1}[s_1(x)]$$

$$- \int_0^1 \int \rho_t(x) \left(\partial_t s \ + \ \tfrac{1}{2} \|\nabla s\|^2 \ + \ \nabla s \cdot v_{\text{prior}} \ + \ \tfrac{1}{2} s^2 \right) dx \, dt. \tag{16}$$

We want to start by minimizing Definition 3.2. Since v_{prior} is constant and known, we only need to minimize the "learned" action portion v_{corr}, then the problem becomes the following:

Consider the velocity–prior guided WFR action:

$$\min_{\rho, \, v_{\text{ot}}, \, g} \quad \mathcal{A}(\rho, v_{\text{corr}}, g) := \int_0^1 \int_\Omega \left(\tfrac{1}{2} \|v_{\text{corr}}(t, x)\|^2 + \tfrac{1}{2} g(t, x)^2 \right) \rho_t(x) \, dx \, dt \tag{17}$$

$$\text{s.t.} \quad \partial_t \rho_t + \nabla \cdot \big(\rho_t(v_{\text{prior}} + v_{\text{corr}}) \big) = g_t \, \rho_t, \qquad \rho_{|t=0} = \rho_0, \ \ \rho_{|t=1} = \rho_1.$$

Step 1: Lagrangian formulation
First, we introduce a scalar multiplier $s(t, x)$, the Lagrangian becomes:

$$\mathcal{L} = \int_0^1 \int_\Omega \left(\tfrac{1}{2} \|v_{\text{corr}}\|^2 + \tfrac{1}{2} g^2 \right) \rho \, dx \, dt \tag{18}$$

$$+ \int_0^1 \int_\Omega s \Big(\partial_t \rho + \nabla \cdot (\rho(v_{\text{prior}} + v_{\text{corr}})) - g\rho \Big) dx \, dt.$$

Step 2: Integration by parts
Integration by parts in time on $\int s \partial_t \rho$

$$\int_0^1 \int_\Omega s \, \partial_t \rho \, dx \, dt = \Big[\int_\Omega s \, \rho \, dx \Big]_{t=0}^{t=1} - \int_0^1 \int_\Omega \rho \, \partial_t s \, dx \, dt \tag{19}$$

$$= \mathbb{E}_{x \sim \rho_0}[s_0(x)] - \mathbb{E}_{x \sim \rho_1}[s_1(x)] - \int_0^1 \int_\Omega \rho \, \partial_t s \, dx \, dt.$$

Integration by parts in space on $\int s \nabla \cdot (\rho w)$ with $w := v_{\text{prior}} + v_{\text{ot}}$

$$\int_\Omega s \, \nabla \cdot (\rho w) \, dx = \int_{\partial\Omega} s \, \rho \, w \cdot n \, d\sigma - \int_\Omega \nabla s \cdot (\rho w) \, dx. \tag{20}$$

Assuming zero boundary flux or fast decay, the boundary term vanishes:

$$\int_0^1 \int_\Omega s \, \nabla \cdot (\rho w) \, dx \, dt = - \int_0^1 \int_\Omega \rho \, w \cdot \nabla s \, dx \, dt. \tag{21}$$

Then, the Lagrangian becomes

$$\mathcal{L} = \mathbb{E}_{x \sim \rho_0}[s_0(x)] - \mathbb{E}_{x \sim \rho_1}[s_1(x)] \tag{22}$$

$$+ \int_0^1 \int_\Omega \rho \left[\tfrac{1}{2} \|v_{\text{corr}}\|^2 - v_{\text{corr}} \cdot \nabla s + \tfrac{1}{2} g^2 - s \, g - \partial_t s - \nabla s \cdot v_{\text{prior}} \right] dx \, dt.$$

Step 3: Fenchel–Young inequality
The Fenchel–Young inequality states that for any vectors a and p, we have:

$$\tfrac{1}{2} \|a\|^2 \geq p \cdot a - \tfrac{1}{2} \|p\|^2 \tag{23}$$

We set $a = v_{\text{corr}}$ and $p = \nabla s$, then we have:

$$\tfrac{1}{2} \|v_{\text{corr}}\|^2 - v_{\text{corr}} \cdot \nabla s \geq -\tfrac{1}{2} \|\nabla s\|^2 \tag{24}$$

Similarly, we set $a = g$ and $p = s$, then we have:

$$\tfrac{1}{2} g^2 - s \, g \geq -\tfrac{1}{2} s^2, \tag{25}$$

with equality iff $v_{\text{ot}} = \nabla s$ and $g = s$. Thus, putting pieces together, we have:

$$\mathcal{A}(\rho, v_{\text{corr}}, g) \ \geq \ \mathbb{E}_{x \sim \rho_0}[s_0(x)] - \mathbb{E}_{x \sim \rho_1}[s_1(x)]$$

$$- \int_0^1 \int \rho_t(x) \left(\partial_t s \ + \ \tfrac{1}{2} \|\nabla s\|^2 \ + \ \nabla s \cdot v_{\text{prior}} \ + \ \tfrac{1}{2} s^2 \right) dx \, dt. \tag{26}$$

B ADDITIONAL EXPERIMENTS

Unbalanced case - Gaussian Translation We create a synthetic gaussian dataset to mimic the cell-fate setting by creating two uneven mass densities with a RNA velocity prior. We set $v_{\text{prior}} = b + \eta(x - \mu_0)$, $b = \mu_1 - \mu_0$ which shift the means with a mild linear drift. By prop.3.1, the learned s_θ models the growth term $g(x) = s_\theta(x)$ to correct the mass imbalance, while $\nabla s_\theta(x)$ adjusts the geometric shape deformation. Fig.2 (right) displays mass-aware hexbins together with 95% covariance ellipses. Our VP-HJF closely aligns its ellipse with the target,indicating the mean and covariance agreement. The light color intensity of the bins indicate the local mass allocation match between the predicted bin masses (blue) and target (orange).

Moreover, we also examined the predicted terminal total mass $\sum_i w_i(1)$ and the ground truth in probability. Ours matches the target unbalanced data mass ratio, whereas AM struggled and failed to adjust mass change. This highlights the need for an explicit mass constraint loss such as L_{mass}. In principle, the unbalanced AM objective in Eq. 4 does allow for mass change, since the growth term $g_t = s_t$ governs $\frac{d}{dt} \log w_t$ while transport is driven by ∇s_t. In practice, however, the model often collapses to the trivial solution $s_t \approx 0$, which preserves the *total* mass, or becomes unstable with exponentially exploding weights. For the trivial case, suppose $\sum_i w_i(0) = 1$, and define $M(t) = \int \rho_t(x)\,dx$. Then $\ln M(1) - \ln M(0) = \int_0^1 \mathbb{E}_{\rho_t}\big[s_t(x)\big]\,dt$. If $s_t \to 0$, this implies $M(1) \approx 1$, consistent with our empirical observations. While such behavior can suffice for local reweighting with zero net growth (as in Neklyudov et al. (2023a), Fig. 7), it fails when the total mass must change.

C LLM USAGE

We used LLM for improve on writing, mainly for checking grammar. We also used LLM for finding relevent and related works.